Frontiers of Information Technology & Electronic Engineering
www.jzus.zju.edu.cn; engineering.cae.cn; www.springerlink.com
ISSN 2095-9184 (print); ISSN 2095-9230 (online)
E-mail: jzus@zju.edu.cn

An improved ROF denoising model based on time-fractional derivative*

Xing-ran LIAO
School of Mathematics, Sichuan University, Chengdu 610065, China
E-mail: xrliao_scu@163.com

Received Feb. 10, 2020; Revision accepted Apr. 1, 2020; Crosschecked May 6, 2020

Abstract: In this study, we discuss mainly the image denoising and texture retention issues. Usually, the time-fractional derivative has an adjustable fractional order to control the diffusion process, and its memory effect can nicely retain the image texture when it is applied to image denoising. Therefore, we design a new Rudin-Osher-Fatemi model with a time-fractional derivative based on a classical one, where the discretization in space is based on the integer-order difference scheme and the discretization in time is the approximation of the Caputo derivative (i.e., Caputo-like difference is applied to discretize the Caputo derivative). Stability and convergence of such an explicit scheme are analyzed in detail. We prove that the numerical solution to the new model converges to the exact solution with the order of $O(\tau^{2-\alpha}+h^2)$, where τ, α, and h are the time step size, fractional order, and space step size, respectively. Finally, various evaluation criteria including the signal-to-noise ratio, feature similarity, and histogram recovery degree are used to evaluate the performance of our new model. Numerical test results show that our improved model has more powerful denoising and texture retention ability than existing ones.

Key words: Improved ROF denoising model; Time-fractional derivative; Caputo derivative; Image denoising
https://doi.org/10.1631/FITEE.2000067 **CLC number:** O241.82

1 Introduction

Noise always occurs in an image, especially in astronomical and medical fields, where researchers need, for example, planet images with texture information to analyze the planet, or X-ray images with sufficient details to examine the pathology of patients. How to remove noise in an image and retain as much texture as possible needs to be studied, because high noise levels may make further research difficult and even lead, in the medical case, doctors to misjudge the patient's physical condition.

The image denoising methods must consider the denoising process, i.e., how to maintain the texture hidden in the noisy images. Over the last two decades, hundreds of denoising algorithms have been built, and they obtained useful denoising results, especially those using partial differential equations (PDEs). One reason for using such a PDE method is that the designer can easily impose geometric constraints in searching for solutions. The most outstanding model is the Rudin-Osher-Fatemi (ROF) total variation based image denoising model (Rudin et al., 1992), which uses a total variation (TV) regularity term and Euler-Lagrange equations to denoise images and can retain the main edges of an image. However, the ROF model may ignore edges with small gradient and texture.

Some improvements on the regularity term for denoising are L_2-norm in Vogel (2002) and L_1-norm in Wu et al. (2019). Both norms have advantages and disadvantages: the L_2-norm can remove noise in the smooth area of an image but cannot retain the edge information, and the L_1-norm can retain the edge but

* Project supported by the National Natural Science Foundation of China (Nos. 61772434 and 61932006)
ORCID: Xing-ran LIAO, https://orcid.org/0000-0003-3721-403X
© Zhejiang University and Springer-Verlag GmbH Germany, part of Springer Nature 2020

leads to a staircase effect and even introduces a false edge. Using the third-order polynomial interpolation, Blomgren et al. (1997) combined the L_1- and L_2-norm to form a new adaptive L_1-L_2-norm regularization term. However, in every iteration of the third-order polynomial interpolation model, the coefficients of the interpolation polynomial should be recalculated. This slows down the calculation, and therefore lowers its efficiency. Blomgren et al. (1997) and Bergounioux and Piffet (2010) proposed the BV2 semi-norm to describe image slick. Bredies et al. (2010) and Knoll et al. (2011) proposed a general and generalized TV to describe image structures. These models use high-order derivatives to depict the smooth components of image segmentation. This can remove the ladder phenomenon well in denoising and maintain the texture of the image, but the disadvantage is that the calculation of high-order derivatives is time-consuming. Therefore, how to preserve the texture and edge information has been the main issue in the past, but why not remove just the noise and finally let the texture information emerge?

It is well-known that the fractional derivative has a memory effect, and to the best of our knowledge, in all the previous works just the space-fractional derivative was used, which cannot effectively control the diffusion process (Abirami et al., 2018; Bai and Feng, 2018). However, in this study, the time-fractional derivative is used in the image denoising model. In our improved time-fractional ROF model, we replace the first-order derivative with a time-fractional derivative and still use the TV norm in the Euler-Lagrange equation to denoise images. Our new model is called the TVF model, and its advantage is that in each iteration of denoising, the noise is first removed and then the image in the previous iteration is added with a specific ratio. In this way, the edge and texture information in the new image is retained. In the end, noise can be removed and texture information emerges. Also, the new numerical scheme can converge to the exact original image with the order of $O(\tau^{2-\alpha}+h^2)$, where τ, α, and h are the time step size, fractional order, and space step size, respectively.

2 ROF model and time-fractional derivative

In this section, we introduce mainly the ROF model proposed by Rudin et al. (1992) and the Euler-Lagrange equations. According to Rudin's model, we denote u as the denoised image and u_0 the noisy image, and assume that u can be recovered as the original image. Then, $u_0=u+\eta$, where η is noise. The TV regularization term can be written as $\mathrm{TV}[u(x, y)]=\iint|\nabla u|\,\mathrm{d}x\mathrm{d}y$, where ∇u is the gradient of u. Here, we consider u as a continuous two-dimensional function. Our target is to minimize

$$\mathrm{TV}[u(x,y)]=\iint|\nabla u|\,\mathrm{d}x\mathrm{d}y \tag{1}$$

with two constraints:

$$\iint u\mathrm{d}x\mathrm{d}y=\iint u_0\mathrm{d}x\mathrm{d}y, \tag{2}$$

$$\iint\frac{1}{2}(u-u_0)^2\,\mathrm{d}x\mathrm{d}y=\sigma^2. \tag{3}$$

In fact, the second constraint means that the variance of noise is σ^2 and that its mean is 0.

$\mathrm{TV}[u(x, y)]$ is a convex function and the necessary conditions of such a functional minimization problem can lead to the Euler-Lagrange equation. We finally arrive at the following equation:

$$-\nabla\left(\frac{\nabla u}{|\nabla u|}\right)+\lambda(u-u_0)=0, \tag{4}$$

where λ is the Lagrange multiplier.

To overcome the singularity of Eq. (4), we rewrite the left side as

$$\begin{aligned}&-\nabla\left(\frac{\nabla u}{\sqrt{|\nabla u|^2+\beta}}\right)+\lambda(u-u_0)\\&=\frac{(u_x^2+\beta)u_{yy}+(u_y^2+\beta)u_{xx}-2u_xu_y}{(u_x^2+u_y^2+\beta)^{3/2}}+\lambda(u-u_0),\end{aligned} \tag{5}$$

where β is a constant to prevent the denominator from being 0 (usually $\beta=10^{-5}$).

By applying the gradient-projection method (Rosen, 1961), the ROF model is expressed as

$$\frac{\partial u}{\partial t}=\nabla\left(\frac{\nabla u}{|\nabla u|}\right)-\lambda(u-u_0). \tag{6}$$

Note that λ varies with t. When this dynamic system becomes stable, i.e., $\partial u/\partial t=0$, we can obtain

$$\lambda=-\frac{1}{2\sigma^2}\int\left(\sqrt{u_x^2+u_y^2}-\frac{(u_0)_x u_x+(u_0)_y u_y}{\sqrt{u_x^2+u_y^2}}\right)\mathrm{d}x\mathrm{d}y. \tag{7}$$

In our new model, we substitute $\partial u/\partial t$ by ${}_0^{\mathrm{C}}D_t^{\alpha}u(x, t)$, which denotes the Caputo time-fractional derivative. Its definition is given as

$${}_0^{\mathrm{C}}D_t^{\alpha}u(x,t)=\frac{1}{\Gamma(1-\alpha)}\int_0^t(t-\eta)^{-\alpha}\frac{\partial u(x,\eta)}{\partial\eta}\mathrm{d}\eta, \tag{8}$$

where Γ is the Gamma function, α the order of fractional derivative, and η the integral parameter.

From the definition of the Caputo time-fractional derivative, we find that the value of the Caputo derivative at each point is the weighted average of the previous points with the weight of $1/\Gamma(2-\alpha)$, where $\alpha\in(0, 1]$. Such properties can help a lot when we design a specific scheme, because we can iterate algorithms many times and control the gray value of the image on [0, 255]. As a result, our improved ROF model can be rewritten as

$${}_0^{\mathrm{C}}D_t^{\alpha}u(x,t)=\nabla\left(\frac{\nabla u}{|\nabla u|}\right)-\lambda(u-u_0). \tag{9}$$

Denoising the image is to solve PDE (9). Thus, a discretization method must be designed to derive numerical solutions.

3 Discretization method for time-fractional differential equations

In this section, we design a discretization method for PDE (9), where we apply an integer-order difference method for space direction and a Caputo-like difference method (Podlubny, 1998) for time direction.

For the time direction difference, let

$$t_k=k\tau,\quad k=0, 1, \ldots, K, \tag{10}$$

where $\tau=T/K$ is the time step, T the termination time, and K the number of equal parts of the time area. We use the Caputo-like difference method (Podlubny, 1998) to approximate the original Caputo derivative. Hence, we have

$${}_0^{\mathrm{C}}D_t^{\alpha}u(t_{k+1})=\frac{\tau^{-\alpha}}{\Gamma(2-\alpha)}\sum_{n=0}^{k}b_k[u(t_{k-n+1})-u(t_{k-n})]+\tilde{R}_{k+1}, \tag{11}$$

where b_k (k=0, 1, …, K) are the coefficients of each term and

$$\begin{cases}1=b_0>b_1>\ldots>b_k,\quad b_n\to 0\ \text{as}\ n\to\infty,\\ \sum_{j=0}^{k}(b_j-b_{j+1})+b_{k+1}=1.\end{cases} \tag{12}$$

The truncation error of such a Caputo difference method is $|\tilde{R}_{k+1}|\le C\tau^{2-\alpha}$, where C is a constant.

For the space direction difference, we suppose that the space variables x and y satisfy $x, y\in[0, l]\times[0, l]$, where l is the side length of the image. Here, x and y represent the length and width of the image, respectively. We discretize the space domain by placing a grid on the spatial axis with the grid spacing h. We introduce the notations as

$$x_i=ih,\ y_j=jh,\ i,j=0,1,\cdots,M,$$

where $h=l/M$ and M is the number of subparts of the spatial length of an image.

Let $u(x, t)$ be defined on $\Omega\times[0, T]$, where Ω is the image space. For an array $u_{i,j}^k$ (i, j=0, 1, …, M, k=0, 1, …, K), we denote

$$\begin{cases}\delta_x u_{i,j}^k\triangleq u_x\big|_{i,j}^n=\dfrac{u_{i+1,j}^k-u_{i-1,j}^k}{2h},\\ \delta_y u_{i,j}^k\triangleq u_y\big|_{i,j}^n=\dfrac{u_{i,j+1}^k-u_{i,j-1}^k}{2h},\\ \delta_{xx}^2 u_{i,j}^k\triangleq u_{xx}\big|_{i,j}^n=\dfrac{u_{i+1,j}^k-2u_{i,j}^k+u_{i-1,j}^k}{h^2},\\ \delta_{yy}^2 u_{i,j}^k\triangleq u_{yy}\big|_{i,j}^n=\dfrac{u_{i,j+1}^k-2u_{i,j}^k+u_{i,j-1}^k}{h^2},\\ \delta_{xy}^2 u_{i,j}^k\triangleq u_{xy}\big|_{i,j}^n=\dfrac{u_{i+1,j}^k-u_{i-1,j}^k-u_{i,j+1}^k+u_{i,j-1}^k}{4h^2},\end{cases} \tag{13}$$

where δ is the central difference operator.

Hence, using the above discretization of time and space directions, we can derive the following fractional-order explicit difference scheme:

$$u_{i,j}^{k+1}=u_{i,j}^{k}-\sum_{n=1}^{k}b_n(u_{i,j}^{k-n+1}-u_{i,j}^{k-n})+\mu\left(\frac{S_{i,j}^{n}}{V_{i,j}^{n}}-\lambda u_{i,j}^{n}+\lambda u_0\right), \tag{14}$$

where i, j=0, 1, …, M, k=0, 1, …, K, $\mu=\tau^{\alpha}\Gamma(2-\alpha)$, and

$$\begin{aligned}S_{i,j}^{k}=&[(\delta_x u_{i,j}^{k})^2+\beta](\delta_{yy}^2 u_{i,j}^{k})+[(\delta_y u_{i,j}^{k})^2+\beta]\\&\cdot(\delta_{xx}^2 u_{i,j}^{k})-2(\delta_x u_{i,j}^{k})(\delta_y u_{i,j}^{k})(\delta_{xy}^2 u_{i,j}^{k}),\end{aligned} \tag{15}$$

$$V_{i,j}^{k}=[(\delta_x u_{i,j}^{k})^2+(\delta_y u_{i,j}^{k})^2+\beta]^{3/2}. \tag{16}$$

4 Analysis of stability and convergence

In this section, we analyze the stability of Eq. (14). Let $\boldsymbol{V}=(\boldsymbol{V}_1, \boldsymbol{V}_2, \ldots, \boldsymbol{V}_M)$, $\boldsymbol{W}=(\boldsymbol{W}_1, \boldsymbol{W}_2, \ldots, \boldsymbol{W}_M)$, with $\boldsymbol{V}_i=(V_{1,i}, V_{2,i}, \ldots, V_{M,i})$ and $\boldsymbol{W}_i=(W_{1,i}, W_{2,i}, \ldots, W_{M,i})$ (i=0, 1, …, M) being vectors of the real Euclidean space $\mathbb{R}^{M-1}\times\mathbb{R}^{M-1}$, and define

$$\begin{cases}(\boldsymbol{V},\boldsymbol{W})=\sum_{i=0}^{M}\sum_{j=0}^{M}V_{i,j}W_{i,j}\Delta x\Delta y,\\ \|\boldsymbol{V}\|_2=(\boldsymbol{V},\boldsymbol{V})^{1/2}=\left(\sum_{i=0}^{M}\sum_{j=0}^{M}V_{i,j}^2h^2\right)^{1/2}.\end{cases} \tag{17}$$

Suppose that $\tilde{u}_{i,j}^{k}$ (i, j=0, 1, …, M, k=0, 1, …, K) is the approximate solution to Eq. (14). The error $\varepsilon_{i,j}^{k}=u_{i,j}^{k}-\tilde{u}_{i,j}^{k}$ satisfies

$$\begin{aligned}\varepsilon_{i,j}^{k+1}=&(1-b_1)\varepsilon_{i,j}^{k}+\sum_{n=1}^{k-1}(b_n-b_{n+1})\varepsilon_{i,j}^{k-n}+b_k\varepsilon_{i,j}^{0}\\&+\mu\left[g(u_{i,j}^{k})-g(\tilde{u}_{i,j}^{k})-\lambda\varepsilon_{i,j}^{k}\right],\end{aligned} \tag{18}$$

where

$$\begin{cases}g(u_{i,j}^{k})=(\delta_{xx}^2u_{i,j}^{k})A_{i,j}^{k}-(\delta_{xy}^2u_{i,j}^{k})C_{i,j}^{k}+(\delta_{yy}^2u_{i,j}^{k})B_{i,j}^{k},\\ A_{i,j}^{k}=\dfrac{(\delta_y u_{i,j}^{k})^2+\beta}{V_{i,j}^{k}},\\ B_{i,j}^{k}=\dfrac{(\delta_x u_{i,j}^{k})^2+\beta}{V_{i,j}^{k}},\\ C_{i,j}^{k}=\dfrac{2(\delta_x u_{i,j}^{k})(\delta_y u_{i,j}^{k})}{V_{i,j}^{k}}.\end{cases} \tag{19}$$

Note that $g(\cdot)$ is continuous and is differentiable on $u_{i,j}^{k}$ (here, g has three hidden variables). Hence, there must exist a constant L such that

$$\left|g(u_{i,j}^{k})-g(\tilde{u}_{i,j}^{k})\right|\le L\left|\varepsilon_{i,j}^{k}\right|. \tag{20}$$

Multiplying Eq. (18) by $\varepsilon_{i,j}^{k+1}$ and summing it up for both i and j from 1 to M–1, we have

$$\begin{aligned}\|\boldsymbol{E}^{k+1}\|_2^2=&(1-b_1)(\boldsymbol{E}^{k+1},\boldsymbol{E}^{k})+\sum_{n=1}^{k-1}(b_n-b_{n+1})(\boldsymbol{E}^{k-n},\boldsymbol{E}^{k+1})\\&+b_k(\boldsymbol{E}^{0},\boldsymbol{E}^{k+1})-\mu\lambda(\boldsymbol{E}^{k+1},\boldsymbol{E}^{k})\\&+\mu\left[g(u_{i,j}^{k})-g(\tilde{u}_{i,j}^{k}),\boldsymbol{E}^{k+1}\right].\end{aligned} \tag{21}$$

By the Cauchy inequality, we have

$$(\boldsymbol{E}^{k-n},\boldsymbol{E}^{k+1})\le\frac{1}{2}\left(\|\boldsymbol{E}^{k-n}\|_2^2+\|\boldsymbol{E}^{k+1}\|_2^2\right),$$

where n=1, 2, …, k. Furthermore, we have

$$\begin{aligned}\|\boldsymbol{E}^{k+1}\|_2^2\le&\frac{1-b_1}{2}\left(\|\boldsymbol{E}^{k+1}\|_2^2+\|\boldsymbol{E}^{k}\|_2^2\right)\\&+\frac{1}{2}\sum_{n=1}^{k-1}(b_n-b_{n+1})\left(\|\boldsymbol{E}^{k-n}\|_2^2+\|\boldsymbol{E}^{k+1}\|_2^2\right)\\&+\frac{b_k}{2}\|\boldsymbol{E}^{k+1}\|_2^2+\frac{b_k}{2}\|\boldsymbol{E}^{0}\|_2^2\\&+\frac{\mu\lambda+\mu L}{2}\left(\|\boldsymbol{E}^{k+1}\|_2^2+\|\boldsymbol{E}^{k}\|_2^2\right).\end{aligned} \tag{22}$$

Note that $\sum_{n=0}^{k-1}(b_n-b_{n+1})=b_0-b_k=1-b_k$. Then we have

$$\begin{aligned}&\|\boldsymbol{E}^{k+1}\|_2^2\\&\le\frac{1-b_1}{2}\left(\|\boldsymbol{E}^{k+1}\|_2^2+\|\boldsymbol{E}^{k}\|_2^2\right)-\frac{1}{2}\|\boldsymbol{E}^{k+1}\|_2^2\\&\quad+\frac{1}{2}\sum_{n=1}^{k-1}(b_n-b_{n+1})\|\boldsymbol{E}^{k-n}\|_2^2+\frac{b_k}{2}\|\boldsymbol{E}^{0}\|_2^2\\&\quad+\frac{\mu\lambda}{2}\left(\|\boldsymbol{E}^{k+1}\|_2^2+\|\boldsymbol{E}^{k}\|_2^2\right)+\frac{\mu L}{2}\left(\|\boldsymbol{E}^{k+1}\|_2^2+\|\boldsymbol{E}^{k}\|_2^2\right)\\&\le\frac{1+b_1}{2}\|\boldsymbol{E}^{k}\|_2^2+\frac{1}{2}\sum_{n=1}^{k-1}b_n\|\boldsymbol{E}^{k-n}\|_2^2-\frac{1}{2}\sum_{n=1}^{k}b_n\|\boldsymbol{E}^{k-n+1}\|_2^2\\&\quad+\frac{b_k}{2}\|\boldsymbol{E}^{0}\|_2^2+\frac{\mu(\lambda+L)}{2}\left(\|\boldsymbol{E}^{k+1}\|_2^2+\|\boldsymbol{E}^{k}\|_2^2\right).\end{aligned} \tag{23}$$

Due to the inequality of $b_n \geq b_n+1$ (n=0, 1, …, k), we then have

$$\begin{aligned}&\| \boldsymbol{E}^{k+1} \|_2^2 + \frac{1}{2}\sum_{n=1}^{k} b_n \| \boldsymbol{E}^{k+1-n} \|_2^2 \\ \leq &\| \boldsymbol{E}^{k} \|_2^2 + \frac{1}{2}\sum_{n=1}^{k-1} b_n \| \boldsymbol{E}^{k-n} \|_2^2 \\ &+ \frac{\mu(\lambda+L)}{2}\left(\| \boldsymbol{E}^{k+1} \|_2^2 + \| \boldsymbol{E}^{k} \|_2^2\right).\end{aligned} \tag{24}$$

Defining

$$\rho_k = \| \boldsymbol{E}^{k} \|_2^2 + \frac{1}{2}\sum_{n=1}^{k-1} b_n \| \boldsymbol{E}^{k-n} \|_2^2, \tag{25}$$

we have

$$\left[1-\frac{\mu(\lambda+L)}{2}\right]\rho_{k+1} \leq \left[1+\frac{\mu(\lambda+L)}{2}\right]\rho_k + b_k\rho_0. \tag{26}$$

We can always choose $\mu<2/(\lambda+L)$. So, there must exist two positive constants M_2 and Q such that

$$\rho_{k+1} \leq M_2\rho_k + Q\rho_0. \tag{27}$$

Thereby, there exists a constant C_1 such that

$$\| \boldsymbol{E}^{k} \|_2^2 \leq \rho_k \leq C_1 \| \boldsymbol{E}^{0} \|_2^2 . \tag{28}$$

The following theorems of stability can be obtained:

Theorem 1 Assuming that

$$\tau^{\alpha} < \frac{2}{(\lambda+L)\Gamma(2-\alpha)}, \tag{29}$$

the numerical scheme defined by Eq. (14) is stable.

We analyze the convergence of Eq. (14). Let $u(x_i, y_j; t_k)$ (i, j=0, 1, …, M, k=0, 1, …, K) be the exact solution to PDE (9) at the mesh point $(x_i, y_j; t_k)$. Define $\eta_{i,j}^k = u(x_i, y_j; t_k) - u_{i,j}^k$ and $\boldsymbol{Y}^k = (\eta_{i,j}^k)$ (i, j=1, 2, …, M−1, k=1, 2, …, K). Substituting $u_{i,j}^k = u(x_i, y_j; t_k) - \eta_{i,j}^k$ into Eq. (21) leads to

$$\begin{aligned}\eta_{i,j}^{k+1} = &(1-b_1)\eta_{i,j}^k - \sum_{n=1}^{k-1}(b_n - b_{n+1})\eta_{i,j}^{k-n} + b_k\eta_{i,j}^0 \\ &+ \mu\left[g(u_{i,j}^k) - g(\tilde{u}_{i,j}^k) - \lambda\eta_{i,j}^{k+1}\right] + R_{k+1},\end{aligned} \tag{30}$$

where R_k is the truncation error of the kth time layer.

Similar to the above deduction, let

$$\rho_k = \| \boldsymbol{Y}^{k} \|_2^2 + \sum_{n=1}^{k-1} b_n \| \boldsymbol{Y}^{k-n} \|_2^2. \tag{31}$$

Hence, we have

$$\begin{aligned}\left[1-\frac{\mu(\lambda+L)}{2}\right]\rho_{k+1} \leq &\left[1+\frac{\mu(\lambda+L)}{2}\right]\rho_k + b_k\rho_0 \\ &+ C_1(\tau^{2-\alpha}+h^2)^2,\end{aligned} \tag{32}$$

i.e.,

$$\rho_{k+1} \leq \frac{1+\dfrac{\mu(\lambda+L)}{2}}{1-\dfrac{\mu(\lambda+L)}{2}}\left[\rho_k + \tilde{C}(\tau^{2-\alpha}+h^2)^2\right]. \tag{33}$$

Then, there exists a positive constant C_2 such that

$$\| \boldsymbol{Y}^{k} \|_2^2 \leq \rho_k \leq C_2(\tau^{2-\alpha}+h^2)^2. \tag{34}$$

Theorem 2 Suppose that the continuous PDE (9) has a smooth solution $u(x, y; t) \in C^{4,2}(\Omega\times[0, T])$ ($C^{4,2}$ is a space with continuous fourth derivative in space direction and continuous second derivative in time direction) and that condition (29) holds. Then, there exists a positive constant C_2>0 such that

$$\| \boldsymbol{Y}^{k} \|_2 \leq C_2(\tau^{2-\alpha}+h^2). \tag{35}$$

The numerical scheme defined by Eq. (14) is convergent.

5 Numerical tests and result assessments

5.1 Criterion establishment

In this subsection, we compare our new model with traditional ones and use the signal-to-noise ratio (SNR), feature similarity (FSIM) (Zhang et al., 2011), and histogram recovery degree to evaluate the difference between the improved TVF model and the traditional ones.

SNR is used to digitalize the noise in images. Its definition is expressed as follows:

$$\text{SNR} = 10\lg\frac{\sum_{i,j} U_{i,j}^2}{\sum_{i,j}(\overline{U}_{i,j} - U_{i,j})^2}, \tag{36}$$

where $U_{i,j}$ is the original image and $\overline{U}_{i,j}$ the denoised image. Usually, the larger the SNR, the better the denoised image. However, when SNR cannot reflect the texture and edge retention results, another index needs to be built. Under this circumstance, we choose the FSIM index (Zhang et al., 2011), which uses energy to evaluate the similarity between the denoised and original images. Zhang et al. (2011) proved that it can reflect the denoising results more objectively than the SNR index. For its definition, readers can refer to Zhang et al. (2011).

The histogram recovery degree, obtained by comparison of the histograms of the original and denoised images, shows in which gray value the information is lost. A good denosing model will recover histogram of an original image as much as possible.

5.2 Comparisons of images with texture and edge information

In this subsection, comparisons are made between images with the Gauss filter, traditional ROF, PM anisotropic diffusion (Bai and Feng, 2018), and our improved TVF model. The ROF model and PM anisotropic model are the most important ones since the 1980s, and are the bases of many subsequent research works on removing noise using PDEs. To illustrate our model's advantages, we use not only three kinds of images, but also our criteria built in Section 5.1. For the Gauss filter, we set it as the representative of other noise reduction algorithms.

We choose three types of images: the first has simple texture and edge information, like a standard cameraman image; the second has medium complex texture and edge information, like the pirate image; the third has complex texture and edge information. For such complex images, we use not only a standard test image like the mandrill image, but also a Moon surface image. Results illustrate that our improved model can obtain as good results as the traditional models for the first type and much better results for the second and third types.

Without a specific illustration in this subsection, all the image sizes are 512×512, and we add Gaussian noise with σ^2=255. The mask of the Gauss filter is 3×3 and the variance of noise is σ^2=255. In the ROF model (Rudin et al., 1992), we choose τ=0.2, λ_0=0 (the first λ), and β=1. In the PM model, we choose the integral constant τ=1/7, smoothness control coefficient K=5, and the conductivity function

$$-C(x,y,t)=\frac{1}{1+\exp[-(\lambda/K)^2]},$$

where λ is a constant. For our time-fractional scheme, we choose the first five terms of the Caputo difference in Eq. (14) and α=0.5.

The denosing results of the cameraman image are shown in Fig. 1.

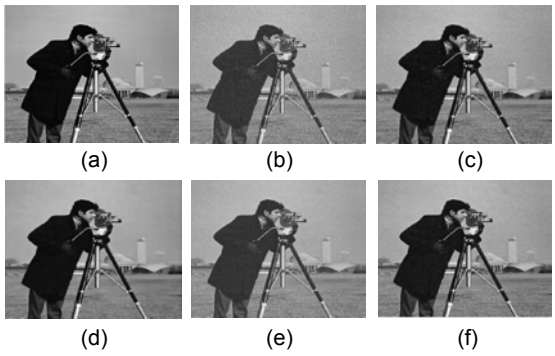

Fig. 1 Comparison results of the cameraman image: (a) original image; (b) noisy image; (c) results of the Gauss filter; (d) results of the ROF model; (e) results of the PM model; (f) results of our TVF model

All algorithms can obtain good results on this image with simple texture and edge information, and the differences in the results of the histogram recovery degree, SNR, and FSIM are acceptable. So, we conclude that when dealing with an image with simple texture, our improved model can act as a traditional model. Results of histogram recovery, SNR, and FSIM are shown in Fig. 2, Table 1, and Table 2, respectively.

From Fig. 2, we see that the Gauss filter loses a lot of information in the low gray part and that the ROF model does not recover the original image very well. Although the PM model obtains better results than the ROF model and Gauss filter, our improved model is even better than the PM model. From the results of SNR and FSIM, we can also conclude that our improved model is the best.

The pirate image has a medium degree of texture and edge information, focusing on the pirate hair, hat, headwear, and face. From the denoising results, we find that the ROF and PM models blur much textural information, while in our improved model such texture is maintained. A similar conclusion can be

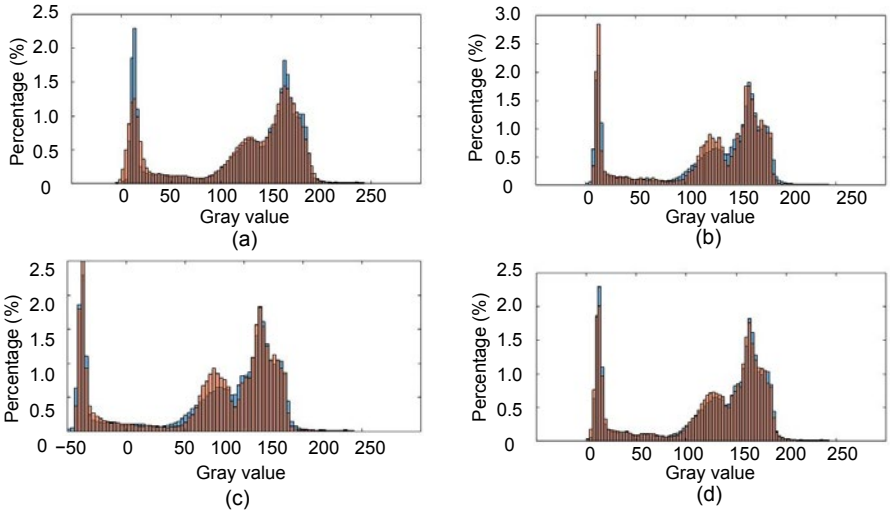

Fig. 2 Histogram recovery results of the cameraman image: (a) Gauss filter; (b) ROF model; (c) PM model; (d) our TVF model

The blue part is the histogram of the original image and the red part is the histogram of the denoising model. References to color refer to the online version of this figure

Table 1 Signal-to-noise ratio (SNR) comparison results

Image	SNR			
	Gauss filter	ROF model	PM model	TVF model
Cameraman	60.0403	60.5025	56.9834	**62.8497**
Pirate	52.2042	51.9992	52.1350	**55.2822**
Mandrill	**52.5417**	44.4835	44.9300	52.5372
Moon	37.0084	35.6946	38.5749	**41.2559**

Bold font emphasizes the model with the largest SNR value of the denoising results in each experiment

Table 2 Feature similarity (FSIM) comparison results

Image	FSIM			
	Gauss filter	ROF model	PM model	TVF model
Cameraman	0.9406	0.9344	0.9538	**0.9584**
Pirate	0.9467	0.9224	0.9268	**0.9550**
Mandrill	**0.9588**	0.8478	0.8498	0.9528
Moon	0.9261	0.8840	0.9080	**0.9319**

Bold font emphasizes the model with the largest FSIM value of the denoising results in each experiment

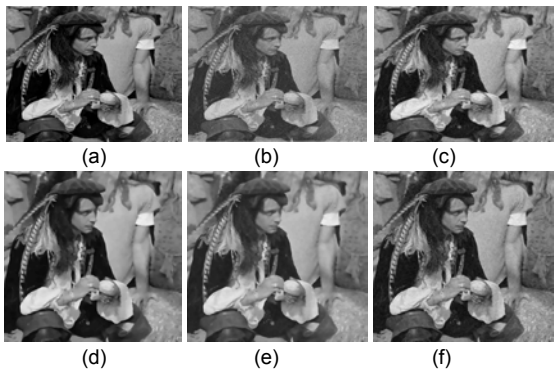

Fig. 3 Comparison results of the pirate image: (a) original image; (b) noisy image; (c) results of the Gauss filter; (d) results of the ROF model; (e) results of the PM model; (f) results of our TVF model

obtained from the results of histogram recovery, SNR, and FSIM.

As we can see from Figs. 3 and 4, Fig. 3d is the best though some information is lost. From the results of FSIM and SNR, we can see that the new model is the best in reconstructing the original image. Now we find that as the texture information increases, our new model shows its strong ability in small edge and texture recovery.

We test the mandrill image which has complex texture information in the mandrill feather. We can see that the Gauss filter obtains good results, because the noise variance of its mask is set as σ^2=255, which can remove the added Gaussian noise. When the noise type changes, it may easily fail, but we still set it as the denoising standard. Under this standard, we can see that the ROF and PM models lose some feather information, while our improved model can work as efficiently as the Gauss filter.

A similar conclusion is obtained from the results

of histogram recovery, SNR, and FSIM. We find that Fig. 5d matches the best, but its SNR and FSIM are lower than those of the Gauss filter. As we said, the Gauss filter can deal with only specific noise, while our improved model can deal with different noises. Similar results can be obtained from Fig. 6.

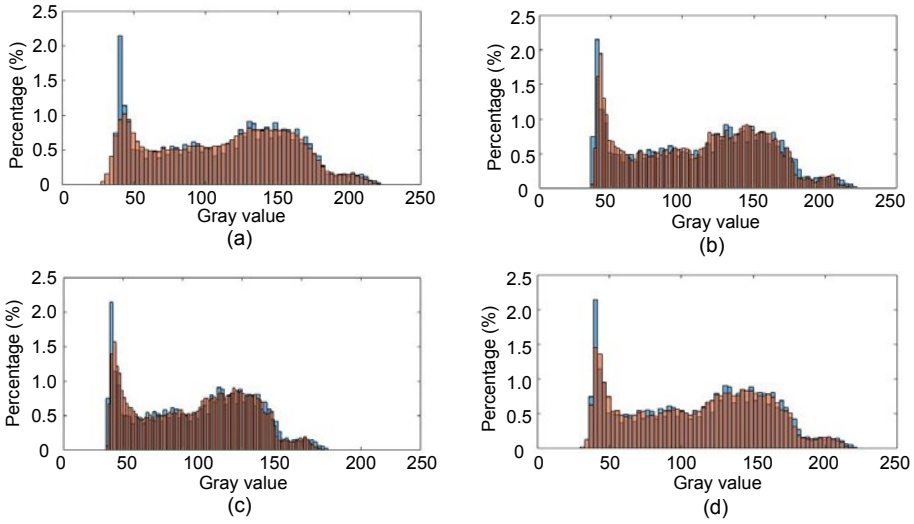

Fig. 4 Histogram recovery results of the pirate image: (a) Gauss filter; (b) ROF model; (c) PM model; (d) our TVF model
The blue part is the histogram of the original image and the red part is the histogram of the denoising model. References to color refer to the online version of this figure

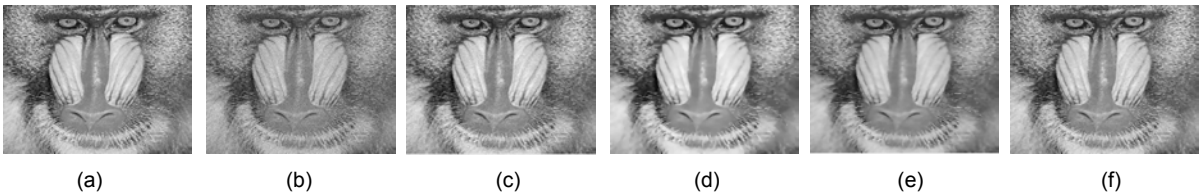

Fig. 5 Comparison results of the mandrill image: (a) original image; (b) noisy image; (c) results of the Gauss filter; (d) results of the ROF model; (e) results of the PM model; (f) results of our TVF model

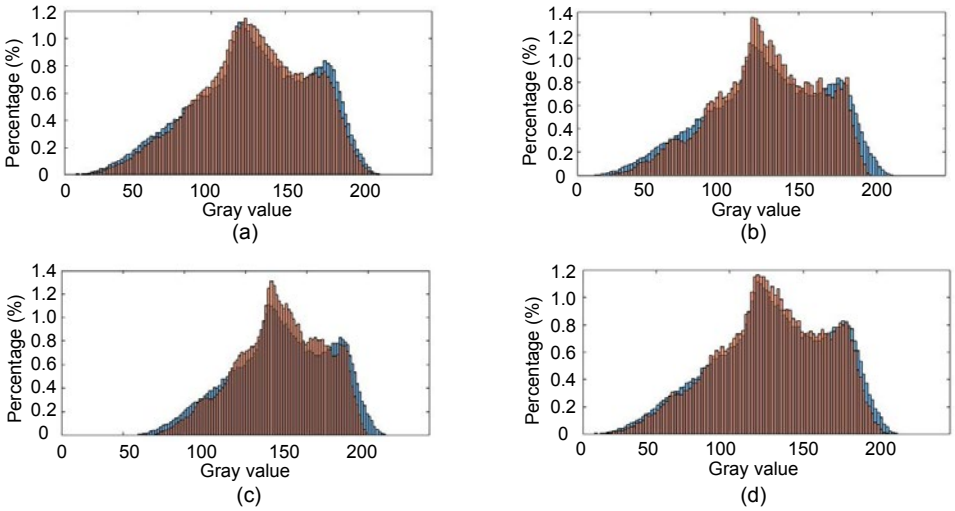

Fig. 6 Histogram recovery results of the mandrill image: (a) Gauss filter; (b) ROF model; (c) PM model; (d) our TVF model
The blue part is the histogram of the original image and the red part is the histogram of the denoising model. References to color refer to the online version of this figure

Next, we test the Moon image. We add Poisson noise with a mean of 400. In Fig. 7d, details of the crater are restored while other algorithms blur it. Specifically, in Figs. 7g and 7h, we zoom in on parts of Figs. 7c and 7f, respectively, and clearly see that Fig. 7f restores small pits on the Moon. While Fig. 7c looks good, these details are actually vague. Such details are important in planetary surface analysis.

We obtain similar results from histogram recovery. We can see that Fig. 8d recovers well in the medium gray part but loses some information in the low gray part. However, noticing that these parts are all in the dark parts of the Moon, such results are acceptable. In terms of SNR and FSIM, we can obtain similar results.

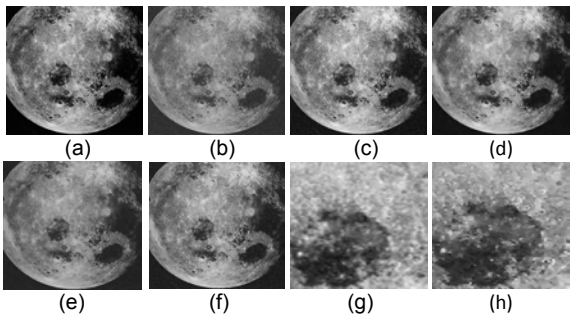

Fig. 7 Comparison results of the Moon image: (a) original image; (b) noisy image; (c) results of the Gauss filter; (d) results of the ROF model; (e) results of the PM model; (f) results of our TVF model; (g) a part of (c); (h) a part of (f)

Based on the above two tests, we can conclude that our new model has better denoising results than the traditional ones for an image with complex texture.

6 Conclusions

In this study, we have shown satisfactory texture retention and denoising ability of our new model in both theoretical and practical ways. The stability and convergence conditions of the numerical algorithms have been given, and tests on the images are closely related to the practical application. However, there are still many issues regarding our new model that we need to consider, e.g., to confirm which truncation term in the time-fractional difference is the best and which fractional order is the best to denoise images. Since our new model has demonstrated such potential, future work on the fractional derivative should lead the traditional ROF model to a new area to achieve better denoising results.

Compliance with ethics guidelines

Xing-ran LIAO declares that he has no conflict of interest.

References

Abirami A, Prakash P, Thangavel K, 2018. Fractional diffusion equation-based image denoising model using CN-GL

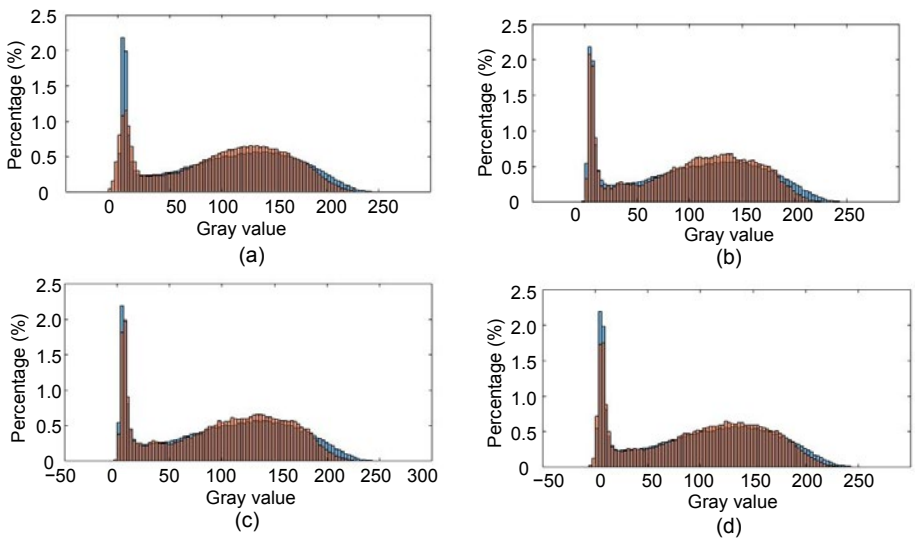

Fig. 8 Histogram recovery results of the Moon image: (a) Gauss filter; (b) ROF model; (c) PM model; (d) our TVF model
The blue part is the histogram of the original image and the red part is the histogram of the denoising model. References to color refer to the online version of this figure

scheme. *Int J Comput Math*, 95(6-7):1222-1239. https://doi.org/10.1080/00207160.2017.1401707

Bai J, Feng XC, 2018. Image denoising using generalized anisotropic diffusion. *J Math Imag Vis*, 60(7):994-1007. https://doi.org/10.1007/s10851-018-0790-4

Bergounioux M, Piffet L, 2010. A second-order model for image denoising. *Set-Valued Var Anal*, 18(3-4):277-306. https://doi.org/10.1007/s11228-010-0156-6

Blomgren P, Chan TF, Mulet P, et al., 1997. Total variation image restoration: numerical methods and extensions. Proc Int Conf on Image Processing, p.384-387. https://doi.org/10.1109/ICIP.1997.632128

Bredies K, Kunisch K, Pock T, 2010. Total generalized variation. *SIAM J Imag Sci*, 3(3):492-526. https://doi.org/10.1137/090769521

Knoll F, Bredies K, Pock T, et al., 2011. Second order total generalized variation (TGV) for MRI. *Mag Reson Med*, 65(2):480-491. https://doi.org/10.1002/mrm.22595

Podlubny I, 1998. Fractional Differential Equations. Academic Press, Cambridge, USA.

Rosen JB, 1961. The gradient projection method for nonlinear programming. Part II. Nonlinear constraints. *J Soc Ind Appl Math*, 9(4):514-532. https://doi.org/10.1137/0109044

Rudin LI, Osher S, Fatemi E, 1992. Nonlinear total variation based noise removal algorithms. *Phys D*, 60(1-4):259-268. https://doi.org/10.1016/0167-2789(92)90242-F

Vogel CR, 2002. Computational Methods for Inverse Problems. SIAM, Philadelphia, USA.

Wu GC, Baleanu D, Bai YR, 2019. Discrete fractional masks and their applications to image enhancement. *In*: Băleanu D, Lopes AM (Eds.), Applications in Engineering, Life and Social Sciences, Part B. De Gruyter, Berlin, Boston, p.261-270. https://doi.org/10.1515/9783110571929

Zhang L, Zhang L, Mou XQ, et al., 2011. FSIM: a feature similarity index for image quality assessment. *IEEE Trans Imag Process*, 20(8):2378-2386. https://doi.org/10.1109/TIP.2011.2109730